On the morphology of radial sand ridges

Zhang Weina[1,2], Zhang Xiaohe[2], Huang Huiming[1], Wang Yigang[1], Fagherazzi Sergio[2]

[1]College of Harbor, Coastal and Offshore Engineering, Hohai University, Nanjing China 210098
[2]Department of Earth and Environment, Boston University, Boston USA 02215

Abstract: We use a hydrodynamic model applied to an idealized fan-shaped basin to explore the morphology and dynamics of radial sand ridges in a convergent coastal system. A positive morphological feedback between channel incision and flow redistribution is responsible for the formation of the channels-ridges pattern. The selection mechanism of bottom wavelength is associated with flow concentration in the deeper part of the channels. Our results are compared to sediment and hydraulic dynamics in the Radial Sand Ridges in China (RSRs). In a convergent, sloping basin the tangentially averaged tidal velocity peaks at 47km from the apex. This distance is similar to the arc distance, 62km, where the RSRs are most incised. An offshore shift in tidal phase results in stronger flows near the north coastline, explaining the presence of asymmetric channel patterns. A numerical stability analysis indicates that small radial oscillations with a wavelength of 10-15 degrees maximize the velocity in the troughs. This oscillation wavelength also emerges in the RSRs, which display a peak in spectral energy at a radial wavelength between 25 to 37.5 degrees. High resolution numerical simulations in the RSRs confirm that flow concentration occurs in the deeper part of the channels, keeping them flushed. We therefore conclude that the RSRs display morphometric characteristics similar to other tidal incisions, like tidal inlets and intertidal channels. This result further supports the dominant role of tidal prism and related peak velocities in incising coastal landscapes.

key words: tide; tidal prism; flow concentration; morphology; tidal channels; rhythmic bedforms;

1 Introduction

Tidal incisions are common in coastal and shallow shelf regions. Networks of channels governed by tides are present in both tidal flats and salt marshes (D'Alpaos et al., 2005; Fagherazzi, 2008; Fagherazzi et al., 1999). Branching channel systems typically occur in short (with respect to the tidal wavelength) and wide tidal basins such as bays and barrier-lagoons (De Swart and Zimmerman, 2009; Marciano et al., 2005). Tidal channels with ebb and flood meanders are also present in elongated, shallow estuaries (Guo, 2014; Hibma et al., 2003).

All these incisions form because a large volume of water is mobilized by tides (tidal prism) and is constrained to flow over a shallow bottom, thus triggering high velocities and scour (Fagherazzi and Furbish, 2001). There is thus a direct relationship between tidal prism and bottom incision, with tidal prism controlling the velocity field and the maximum incision occurring where the velocity peaks. This is well known in tidal inlets, where a relationship between tidal prism and total incision -the cross sectional area of the inlet- is well established (D'Alpaos et al., 2010). Even in tidal flats and salt marshes channel incision is driven by local tidal prism, defined as the water needed to flood and drain the intertidal area related to a specific channel cross section (Fagherazzi and Furbish, 2001; Fagherazzi

et al., 2008; Fagherazzi and Sun, 2004).

The largest tidal incisions in the world are probably the Radial Sand Ridges (RSRs) in the southern Yellow Sea, China (Figure 1). This tidally forced system has rhythmic channels-ridges structures, with radially elongated and widening channels separated by subaerial and subaqueous ridges, in a fan-shaped geometry. The fan-shaped basin is bounded by linear coastlines with an opening angle of 150° (Xu et al., 2016; Zhang et al., 1999; Zhang et al., 2017). Here we want to determine whether the same physical relationships between tidal prism and incision are valid for this large-scale tidal system spanning hundreds of kilometers.

Geological studies indicate that the RSRs formed by the reworking of the Old Yangtze River mouth deposits (Wang et al., 2012; Yang et al., 2002). The intermittent sediment supplied by the Old Yellow River mouth further favored the growth of the RSRs (Wang et al., 2015; Wang et al., 2012). Few studies have been conducted to explain the formation and evolution of the RSRs. Most of them directly link these topographic features to the hydrodynamics induced by tidal waves. The radial tidal flow field is ascribed to the convergent-like tidal wave in the RSRs, generated by the interaction between the rotating tidal wave of the southern Yellow Sea and the progressive tidal wave propagating from the East China Sea, and it is independent of the local topography of the RSRs (Qian et al., 2015; Su et al., 2015; Su et al., 2017). The dominant tidal constituent in the RSRs is the semidiurnal M2 constituent (Su et al., 2015). The tidal flow field of the M2 constituent shows a radial distribution of velocity in line with the axis of the channels during both flood and ebb (Yao et al., 2013). Peak discharges perpendicular to channel cross sections maintain channel stability, preventing silting (Zhang et al., 1999). Numerical simulations show that the radial pattern of the peak flow is persistent, even with a schematized bathymetry obtained by smoothing the local undulations (Zhu and Chang, 2001). Some researchers thus hold that the radial tidal flow field is responsible for the formation and development of the RSRs over long time scales (Qian et al., 2015; Su et al., 2015; Wang et al., 2015; Zhang et al., 1999; Zhu and Chang, 2001). Su et al. (2015) also pointed out that the initial bathymetry of the RSRs influences the magnitude of the tidal flow and is crucial to the formation of channels. Tao et al. (2019) carried out morphodynamic simulations of the RSRs and showed that rhythmic topography can be qualitatively reproduced starting from a smooth sloped bathymetry with M2 tide. However, the understanding of how the incision of channels occurs and why the final configuration of the RSRs is achieved is still lacking. Quantitative analysis of the RSRs bathymetry is an important step for the identification of the morphodynamic processes responsible for these bedforms.

Stability analysis has been widely used to explain the emergence of rhythmic patterns in terrestrial and marine landscapes such as river meanders (Blondeaux and Seminara, 1985; Parker, 1976; Seminara, 1998; Seminara, 2009), estuarine bars (Schramkowski et al., 2002; Schuttelaars and De Swart, 1999), and branching channel patterns in tidal environments (Marciano et al., 2005). In a stability analysis, small-amplitude perturbations are added to the initial bed elevation. These perturbations affect the distribution of bottom shear stresses, hence the erosion and deposition of sediments. The growth rate of perturbations having different frequencies is then evaluated, and the largest rate of growth corresponds to the morphology expected to be observed in the field. A similar numerical analysis is used herein to explore which radial channel wavelength is selected in a convergent coastline.

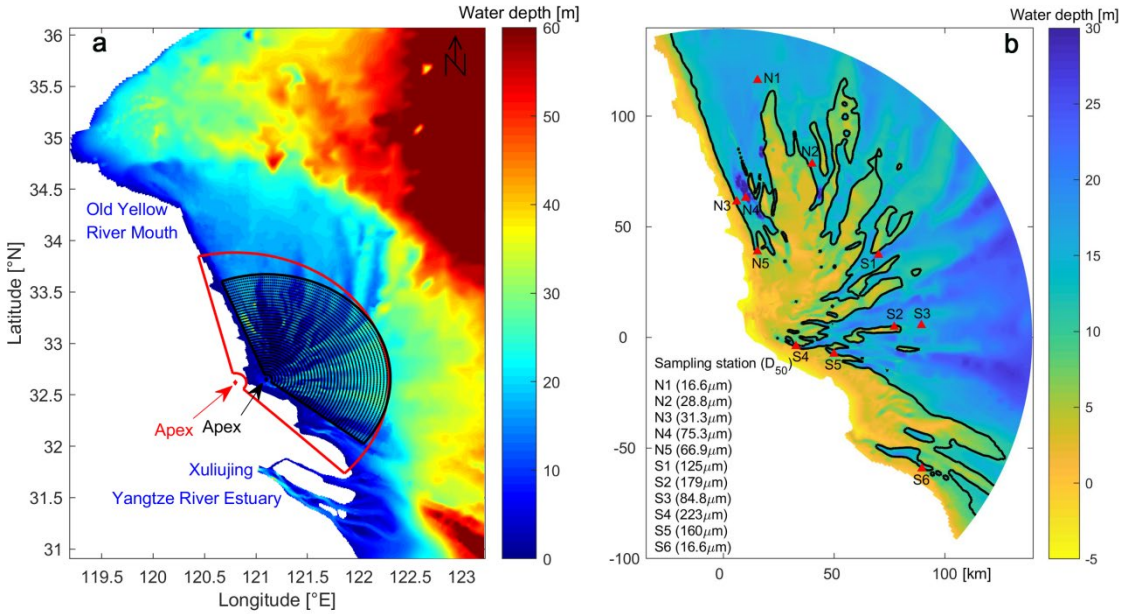

Figure 1. a) Bathymetry and modeling domain. The regional model covers the entire bathymetry of Figure 1a. The black fan-shaped grid shows the area of the bathymetric analysis (Fourier and Wavelet analysis). The red fan-shaped sector shows the nested grid used for the modeling domain of this paper. b) Detail of the modeling domain of Figure 1a. The black line indicates the 10m depth contour line. The red triangles indicate the location of observation stations. The median grain size (D_{50}) of the substrate at the observation stations are shown in the legend.

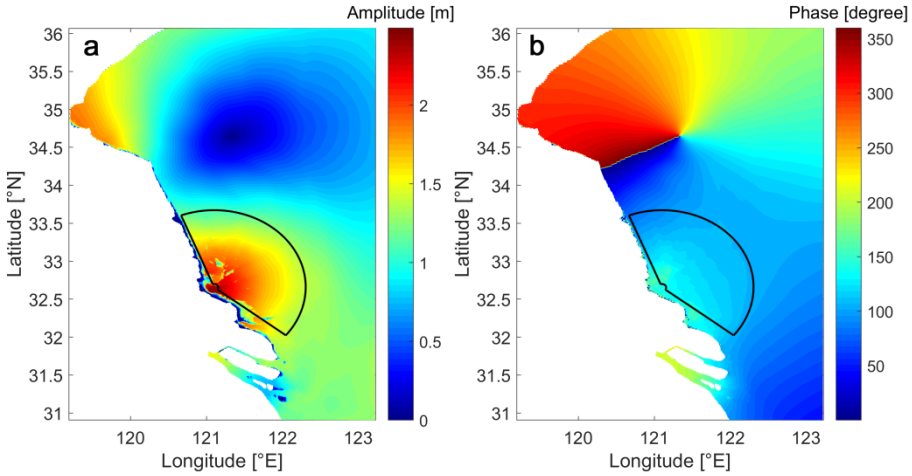

Figure 2. Co-tidal chart of the M2 tide. a) Amplitude of M2 tide. b) Phase of M2 tide. The black fan-shaped sector indicates the boundary of our idealized simulations.

2 Study site

The RSRs is a coastal system with large-scale tidal channels and ridges (Figure 1). The area is near to the Old Yellow River mouth to the north, and borders the Yangtze River estuary to the south. The bed sediment of the RSRs is predominantly constituted by well-sorted sand and silt in offshore areas (Figure 1b), and the clay fraction tends to be distributed more landward over the intertidal flats.

The rotating tidal wave of the southern Yellow Sea and the progressive tidal wave propagating from the East China Sea merge into a standing tidal wave at the offshore boundary of the RSRs that converges toward the shore (Su et al., 2015; Xing et al., 2012). The convergent-like tidal wave is characterized by arc-shaped co-range lines with an early phase in the northern part. The amplitude of the M2 constituent has a mostly uniform value of 1.2m and the phase lag of the M2 constituent varies from 80° to the north (referring to the UTC in this study) to 105° to the south (Figure 2). Because of the topographic convergence, the tidal amplitude increases onshore, reaching a value above 2.0m near the apex of the RSRs. Here we study in detail the bathymetry of the RSRs. The bathymetric data were provided by a coastal investigation and assessment carried out by the Jiangsu Province in 2006 (Mission 908) and updated with field measurements in 2014.

Table 1. Bathymetry settings of idealized simulations.

Scenario	Bottom Slope	Open boundary conditions	Coriolis force
S0-S17	From 0 to 0.00017 every 0.00001	uniform amplitude and phase	No
L1-L9	0.00015 (bottom oscillations)	uniform amplitude and phase	No
LX	0.00015 (single topographic low)	uniform amplitude and phase	No
LXI	0.00015 (two topographic lows)	uniform amplitude and phase	No
AS0-AS17	From 0 to 0.00017 every 0.00001	uniform amplitude, varying phase	Yes
AS15II	0.00015	uniform amplitude and phase	Yes
AS15III	0.00015	uniform amplitude, varying phase	No

3 Methods

3.1 Numerical simulations with idealized geometry

3.1.1 Tidal hydrodynamics

We use the open source modeling system Delft3D-FLOW to simulate tidal hydrodynamics. Delft3D solves the depth-averaged shallow water equations (Van der Wegen and Roelvink, 2008). These equations are discretized on a staggered grid and are solved using the ADI method (Stelling, 1983). At first, we use the numerical model to simulate tidal flow in an idealized fan-shaped basin having flat or gently sloping bottom. In the simulations we flatten the bathymetry for two reasons: i) to better capture the salient interactions between tidal oscillations, tidal prism, and related tidal velocities without the local noise generated by the real bathymetry, and ii) to explore why tidal incisions and radial sand ridges form in a generic sloping bathymetry. As indicated by Murray (2007), a model with reduced complexity is better suited to explain the emergence of morphodynamic features.

The computational domain is a 150° fan-shaped basin with a radius of 113km, mimicking the coastal setting of the RSRs. A small fan-shaped area with a radius of 5km at the basin head is removed from the mesh to prevent numerical instability. The grid resolution is 0.25° in the transverse direction and the aspect ratio of each cell is approximately equal to 1. The water depth at mean sea level is set at 19.6m at the open boundary. This value is the average value of the RSRs bathymetry at 113km from the shore. All the other boundaries are considered impermeable (null normal velocity). The Chézy coefficient is set to 100 $m^{1/2}/s$ based on preliminary calibration of tidal propagation. The eddy viscosity is set to $1m^2/s$ based on Zhou et al. (2014b) and according to grid resolution in the simulations.

In a first set of hydrodynamic simulations we study the effect of bottom slope on the tidal hydrodynamics of our simplified convergent coastline. We keep the water depth at the open boundary fixed and alter the water depth at the apex. The slope ranges from 0 (flat bottom) to 0.00017 (scenario S0-S17 in Table 1). In a second series of simulations we perform a stability analysis to determine what frequency of bottom oscillations is selected during RSRs formation. We therefore introduce small perturbations at the bottom and determine what frequency leads to the highest velocity increase in the troughs. We use a radial, sinusoidal oscillation with amplitude of 1m and angular wavelength of 3°, 6°, 10°, 15°, 25°, 30°, 50°, 75° and 150° (scenario L1-L9 in Table 1). In a third series of simulations we explore the effect of incisions (topographic lows) on the hydrodynamic field and the competition between two topographic lows in order to capture tidal discharge. We prescribe a single topographic low and two topographic lows with the maximum scour depth of 2m and scour length of 30km at the bottom (scenario LX/ LXI in Table 1). The scour length is based on the real bathymetry where high energy bottom oscillations occur. Scour depth of 2m represents a small incision. The result does not qualitatively change if we use 1m or another small incision (small perturbation). These three sets of simulations are forced by the idealized symmetric open boundary conditions. A semidiurnal harmonic tide (M2) with uniform amplitude (1.2m) and phase is prescribed at the arc-shaped open boundary and the Coriolis force is neglected.

Tidal waves are deflected by the Coriolis force in the amphidromic system within an ocean basins (Taylor, 1922). In accordance with the characteristics of the tidal wave in the RSRs, the water level phase lag along the open boundary and the Coriolis force are taken into account in a fourth set of asymmetric hydrodynamic simulations (scenario AS1-AS17 in Table 1). The open boundary is divided into two equal sections. Uniform amplitude (1.2m) and phase (local phase lag 105°) is imposed along the southern half of the open boundary; uniform amplitude (1.2m) and a linearly decreasing phase from 105° at the central point to 80° at the north end is imposed along the north half of the boundary.

3.1.2 Sediment transport

We use scenario LX as an example to test whether concentrated flow with high velocity is responsible for scouring in the topographic low. We also examine what frequency of bottom oscillations leads to the highest erosional trends in the troughs, based on scenario L1-L9.

To quantify the effect of bathymetry on potential depositional and erosional trends, sediment flux divergence is calculated by $Div\ Q = \frac{\partial Q_r}{\partial r} + \frac{1}{r}\frac{\partial Q_\theta}{\partial \theta}$, where $Div\ Q$ is the sediment flux divergence of suspended load or bed load; Q_r and Q_θ indicate sediment flux in the radial and tangential direction.

Mud is transported as suspended load. We use idealized scenario LX and scenario L1-L9 to test the sediment flux divergence of the mud fraction during one tidal cycle. The initial concentration of mud is set to 0.38kg/m^3, similar to the averaged suspended sediment concentrations (SSC) of sampling stations in the RSRs. The erosion and deposition fluxes of mud are calculated applying the Partheniades-Krone formulations (Partheniades, 1965). The critical shear stress for deposition $\tau_{cr,d}$ is set to 1000Pa following Winterwerp et al., (2007); therefore sedimentation is possible throughout the tidal cycle. The critical shear stress for erosion $\tau_{cr,e}$ equals to 0.15Pa in our simulations. The

settling velocity ω_s is specified as 0.0005m/s. The seaward boundary concentration of mud is set to 0kg/m^3.

In the case of sand transport, we follow the approach of Van Rijn (1993) (see also Luan et al., 2017). The median grain size of sand fraction is set to 180μm and the divergence of bed load flux after one tidal cycle is calculated in the scenario LX.

3.2 Numerical simulations with real bathymetry

3.2.1 Model domain and boundary conditions

To perform high resolution simulations with the real bathymetry we use a mesh nested in a regional model for tidal propagation along the Jiangsu coast (Figure 1b). The regional model uses spherical coordinates and spans from 119.2°E to 123.2°E in the longitudinal direction and from 30.9°N to 36.1°N in the latitudinal direction (Figure 1a). The upstream boundary in the Yangtze River estuary is located at Xuliujing Station. Some minor rivers discharge into the sea along the Jiangsu coast. However, most of them have a limited discharge and are thus neglected in our simulations (Yao et al., 2018). The open boundary conditions in the Yellow sea are provided by the globe tide model TPXO 7.2 (Egbert et al., 1994; Egbert and Erofeeva, 2002), and the measured water level at Xuliujing station is set as the upstream boundary conditions in the Yangtze delta. To capture the detailed flow field in the RSRs, high resolution simulations are then preformed on the fan-shaped, Cartesian plane indicated in Figure 1b. The open boundary conditions of the high resolution simulations are generated by the computational results of the regional model.

3.2.2 Sediment composition

The median grain size (D_{50}) of surface bottom samples collected at 11 observation stations are shown in Figure 1b. The northern part of the sand ridges (stations N1-N5) is characterized by finer sediments with respect to the southern part (stations S1-S6). This difference is attributed to different sediment sources that contributed in different periods to the material present in the RSRs. Most of the sand fraction in the RSRs was derived from the paleo-Yangtze River, which entered the sea north of the modern Yangtze estuary. The mud present in the northern part of the RSRs was deposited in the Old Yellow River delta when the Yellow River discharged into the sea in the north Jiangsu coast between 1128 and 1855 (Wang et al., 2012).

For simplicity, in our simulations a spatially uniform distribution of bed fractions is specified in the northern and southern parts. Only two bed fractions are used to represent the composition of bottom sediments: sand fraction with D50 = 180μm and mud fraction with D50 = 20μm. The mass ratio between sand (180μm) and mud (20μm) in each part is specified to match the averaged median grain size of the observation stations. As a result, we assume a bed composition in the northern part with 85% mud and 15% sand, and 42% mud and 58% sand in the southern part.

3.2.3 Model Calibration

We compare simulation results of water level, velocity and suspended sediment concentration to field data at eleven observation stations in the RSRs (Figure 1b). The field data were obtained during

206 a spring tide for the period from 24 August 2006 to 25 August 2006 in intervals of one hour.
207 Following Allen et al. (2007), two parameters are used to evaluate the synthetic performance of
208 the hydrodynamic simulations, the model efficiency:

209 $$ME = 1 - \frac{\sum (D - M)^2}{\sum (D - \overline{D})^2}$$

210 and the root mean squared error:

211 $$RMSE = \sqrt{\sum \frac{(D - M)^2}{n}}$$

212 Where M indicates the simulated result (water level or tidal velocity), D indicates the observation
213 data, $\overline{D}$ is the mean of the observation data, and n is the total number of observations. The value of
214 ME represents model performance, which is classified as follows: $ME > 0.65$ excellent; $0.5 < ME <$
215 0.65 very good; $0.2 < ME < 0.5$ good; $ME < 0.2$ poor. The comparison of time series between measured
216 data and simulated data in four representative stations are shown in Figure 3. We report ME and $RMSE$
217 for water levels and flow velocity magnitude. Overall, the simulated tidal levels and tidal current
218 velocities agree well with the measured data in the RSRs.
219

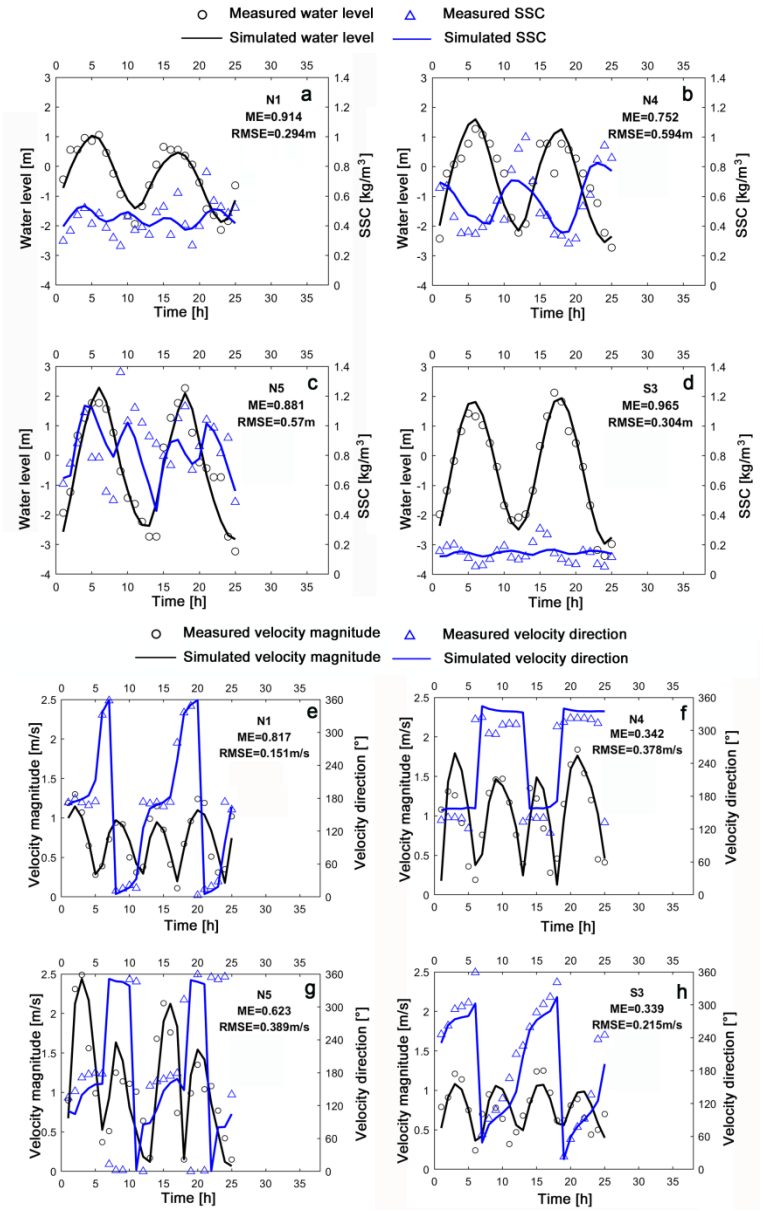

Figure 3. Calibration of water levels and suspended sediment concentrations (SSC) at four representative observation stations (a-d). Calibration of water velocity magnitude and direction (e-h). We report *ME* and *RMSE* for water levels and velocity magnitude in the figures.

220

221 ### 3.3 Bathymetric analysis

222 Discrete Fourier transforms are used to quantify the rhythmic bedforms of the RSRs. Discrete
223 Fourier transform (DFT) operates on discrete signals and is applicable to sampled topographic data of
224 rhythmic surfaces in order to identify periodic structures and reveal features such as wavelength,
225 orientation, and amplitude. The same technique has already been used in terrestrial and marine
226 environments (Cazenave et al., 2013; Perron et al., 2009; Van Dijk et al., 2008). Previous studies
227 applied DFT to a 2D rectangular domain whose sampling data is regularly distributed in even intervals
228 in the x or y direction of a Cartesian plane.

229 Since the RSRs are fan-shaped, we use the DFT in polar coordinates describing each bathymetric

point in terms of radius ρ and angle θ (Figure 1). The locations of the sampling points are distributed in 37 radially uniformly-spaced arcs with a total angle of 150°. We use a triangular interpolation to acquire the bathymetry at every sampling point. The measured bathymetry data points are first organized into a Delaunay triangulation, and then the bathymetry at every sampling point is interpolated. The sampling points are regularly distributed in even intervals of 1° along each arc-shaped transect. We remove the mean value of the sampling data along each arc transect. Spectral analysis based on the 1D DFT is performed on the sampling data along each arc transect. We use wavelet analysis to identify the non-stationary oscillations of the deeply incised channels. A continuous Morlet wavelet is adopted which provides a good trade-off between frequency and spatial precisions (Torrence and Compo, 1998).

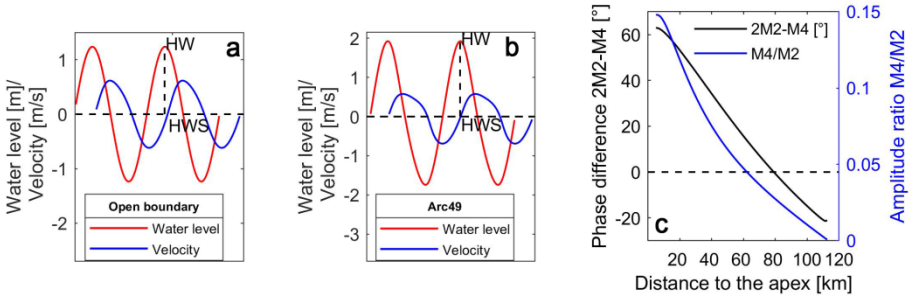

Figure 4. a) Water level and velocity at the open boundary in the scenario S15. b) Water level and velocity at the arc49 located 49km away from the apex. High water (HW) and high water slack (HWS, i.e. when the velocity is zero) are indicated. c) Radial distribution of sea-surface phase difference (2M2-M4), and radial distribution of amplitude ratio M4/M2 in the scenario S15.

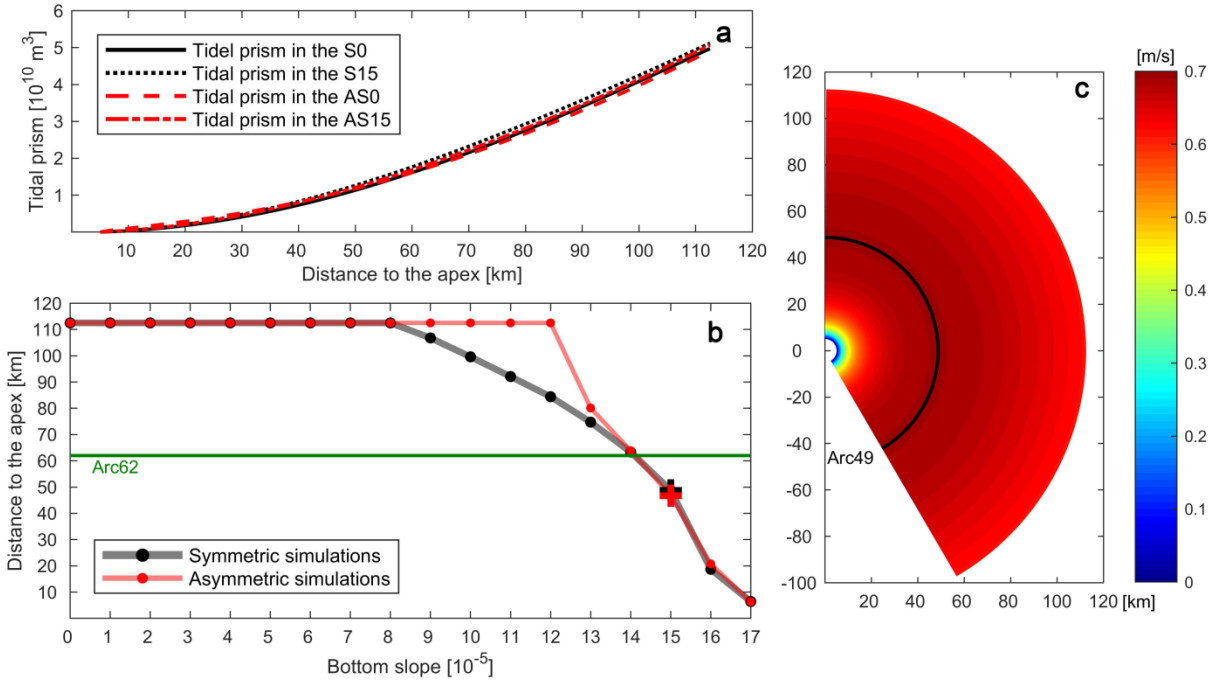

Figure 5. a) Water volume flowing inside/outside each arc transect during a half-tidal cycle

(tidal prism) in the scenarios S0, S15 (black lines) and AS0, AS15 (red lines); b) Relationship between the bottom slope and i) the position of the maximum velocity band in symmetric simulations S1-S17 (black line); ii) the position of maximum tangentially averaged velocity in asymmetric simulations AS1-AS17 (red line). The black cross shows the position of maximum velocity band of S15 and the red cross shows the position of maximum tangentially averaged velocity of AS15 (the scenarios with a slope closest to the averaged slope of the RSRs). The green line shows the position with the highest spectral energy in the DFT. c) Peak velocity distribution in the simulation S15, the maximum velocity band occurs 49 km from the apex.

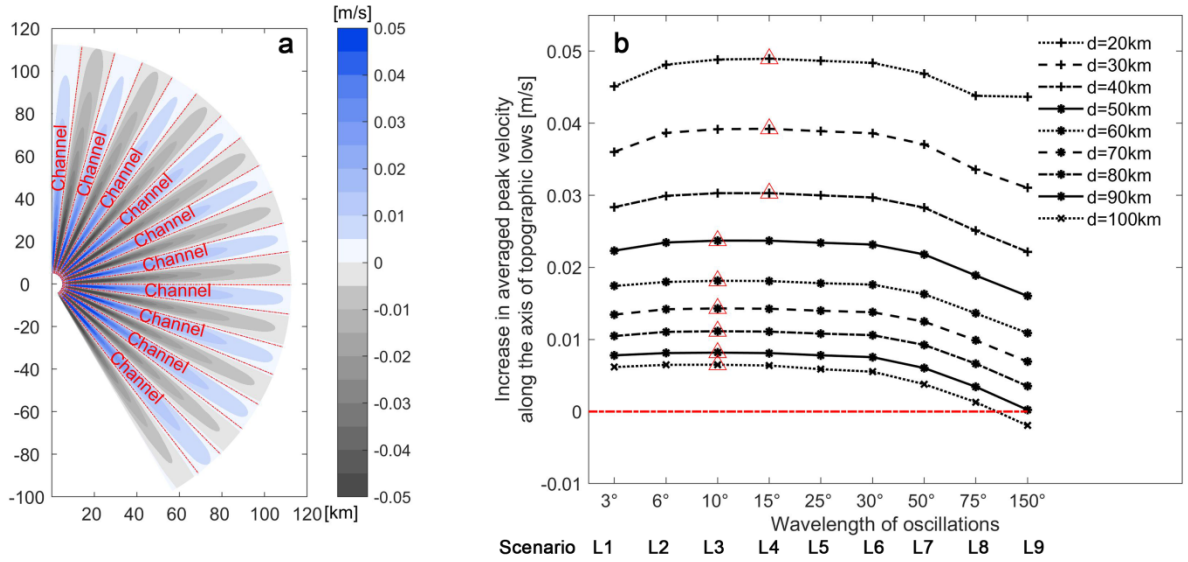

Figure 6. a) Difference in peak velocity between scenario L4 (oscillating bottom) and S15 (planar, sloping bottom). b) Increase in averaged peak velocity along the axis of radial small perturbations (topographic lows of scenarios L1-L9). Red triangles mark the largest velocity increase. Each line shows the velocity increase at a specific distance to the apex.

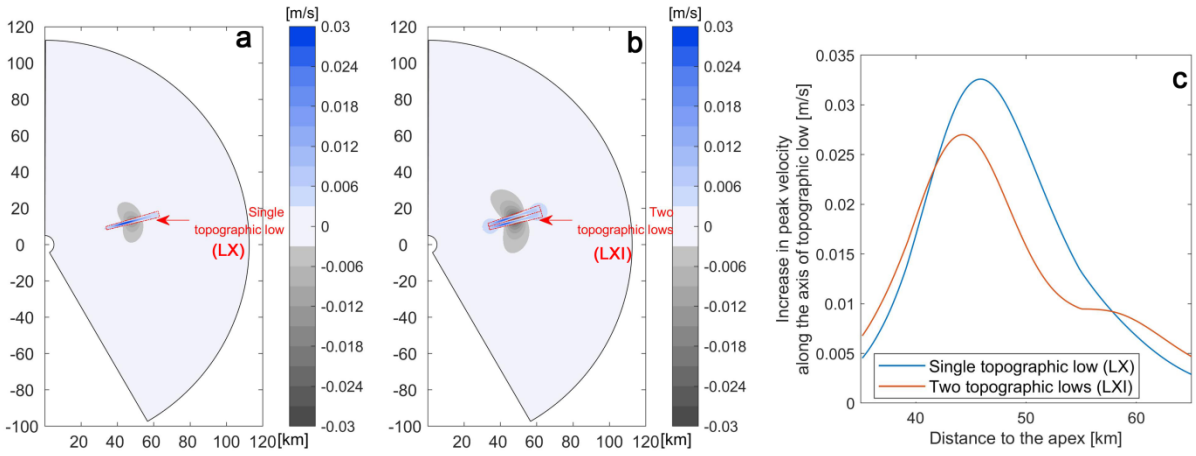

Figure 7. a) Difference in peak velocity between scenario LX (single topographic low) and S15 (planar, sloping bottom). b) Difference in peak velocity between scenario LXI (two topographic lows) and S15 (planar, sloping bottom). c) Increase in peak velocity along the axis of

topographic low (LX versus LXI).

4 Results

4.1 Idealized symmetric flow simulations

The results of the idealized hydrodynamic model indicate that a standing tide is present in the fan-shaped basin. There is a phase shift of almost 90º between water level and velocity fluctuations, with slack water periods occurring at high and low tides, caused by the reflection of the tidal wave at the basin head (Figure 4a, 4b). The tidal flow is characterized by radial currents. The velocity has similar values along each arc, while it varies along the radial direction. Tidal asymmetry is also present, with the sea-surface phase difference (2M2-M4) between 0° to 180° in most areas (Figure 4c), leading to flood domination (Friedrichs and Aubrey, 1988). Tidal distortion decreases offshore, with a decline in M4/M2 ratio in the offshore direction.

Tides are responsible for the exchange of water between the sea and the basin. Figure 5a shows the radial distribution of the water volume flowing inside/outside each arc-shaped transect during half tidal cycle (i.e., the tidal prism). The tidal prism increases in the offshore direction because the basin area increases. Moreover, the tidal prism weakly depends on bottom slope in the scenarios S0-S17, and different bathymetries only lead to slight changes in tidal discharge across a given arc.

We regard the peak flow velocity as the geomorphological agent responsible for channel formation, as commonly assumed in geomorphic studies of tidal systems (D'Alpaos et al., 2005; Friedrichs and Perry, 2001; Myrick and Leopold, 1963). In the case of flat bottom (S0), the peak flow velocity decreases from the open boundary to the basin head because of the reduction in tidal prism. The maximum peak velocity in the entire domain (hereinafter referred to as maximum velocity band) is thus located at the open boundary. As previously described, the tidal prism is almost independent of basin bathymetry. When the bottom slope increases, the water depth decreases inland, so that the velocity must increase to maintain the same tidal discharge. Thus the position of the maximum velocity band moves inside the basin from the open boundary (Figure 5b). The bottom slope strongly influences the peak velocity distribution as well as the location of maximum velocity band. For a bottom slope of 0.00015, similar to the average bottom slope of the RSRs, the maximum velocity band is located 49 km from the apex (Figure 5c). The maximum velocity zone provides the best conditions for the development of tidal channels, because incisions develop faster when the flow is strong (Temmerman et al., 2007).

In the numerical stability analysis, we prescribed small radial perturbations and we determined what frequency results in the largest concentration of flow in the troughs (i.e. the highest increment in velocity). As an example of the impact of an oscillating seabed on hydrodynamics, Figure 6a shows the change in the peak velocity in the scenario L4 (bottom oscillations with wavelength of 15°) versus the planar bed S15. The tidal flow accelerates in topographic lows and decelerates in topographic highs, a mechanism that likely triggers the initiation of rhythmic incisions.

The tidal prism in the case of the oscillating seabed (L1-L9) is identical to the case with planar seabed (S15). However, the water volume conveyed in topographic lows is higher than the volume conveyed in topographic highs, in line with previous findings in tidal channels (Fagherazzi and Furbish, 2001; Fagherazzi et al., 2003). As a result, discharge per unit width is redistributed from topographic highs to topographic lows, increasing the velocity in the troughs and likely leading to more incision.

The seabed oscillations thus likely grow into tidal channels. Since the velocity peaks in our idealized basin at the maximum velocity band, here we expect to find the most incised channels.

The concentration of momentum is different for different wavelengths of bottom oscillations. For an increasing wavelength, the velocity in the troughs first increases and then diminishes. If the wavelength is short, the distance between subsequent topographic lows is too small and they inevitably compete for the same discharge. If the wavelength is long, there is insufficient redistribution of momentum to convey more water to topographic lows. It is important to note that in the distal part the wavelength of the perturbations becomes very large. As a result, flow is no longer concentrated in topographic lows. The velocity can even decrease in depressions because of flow expansion (Figure 6b, scenario L9, d=100km).

To better understand the flow field near an initial scour, a single topographic low was set near the maximum velocity band in a planar, sloping bottom (scenario LX). The magnitude of peak velocity decreases in the area surrounding the initial scour (i.e. dark area in Figure 7a). The tidal flow accelerates in the scour and thus can lead to more local erosion. This single incision thus captures flow and momentum from the nearby topographic highs (the influence area in Figure 7a) to concentrate it in the scour. If a second incision is added in the influence zone, it competes with the first incision, deflecting flow and momentum, thus lowering the velocity in the first incision (Figure 7b, 7c). Incisions too close to each other would thus be unable to concentrate the flow in the scours, because of their overlapping influence zones.

The maximum increase in velocity is reached for a wavelength between 10° to 15° (Figure 6b). This perturbation wavelength therefore grows faster than other perturbations. In a real seabed initial perturbations with all frequencies are likely present. In time the system selects the perturbation that leads to the highest flow concentration, so that this frequency becomes dominant. In fact, incisions related to the dominant wavelength erode more and deepen faster than others. In the long term competition among incisions is in favor of those that increase the velocity the most. Once the dominant oscillations become the most incised, the growth rate of these incisions increases, in a positive feedback (see Fagherazzi and Furbish 2001). Rhythmic channels then form.

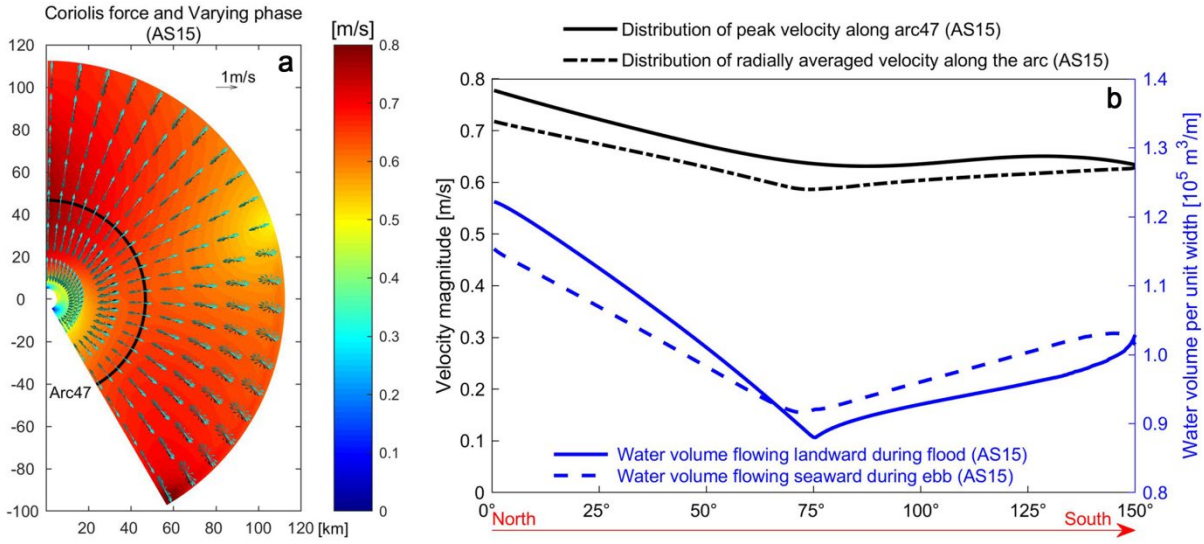

Figure 8. a) Peak velocity distribution in simulation AS15; the black line indicates the arc47 where the maximum value of the tangentially averaged peak velocity occurs (47 km from the

apex). The tidal current vectors are displayed as arrows. b) Distribution of i) radially averaged velocity along the arc (black dash line); ii) peak velocity along arc47 (black solid line); iii) radially averaged water volume per unit width flowing landward during flood (solid blue line) and seaward during ebb (dotted blue line) in simulation AS15.

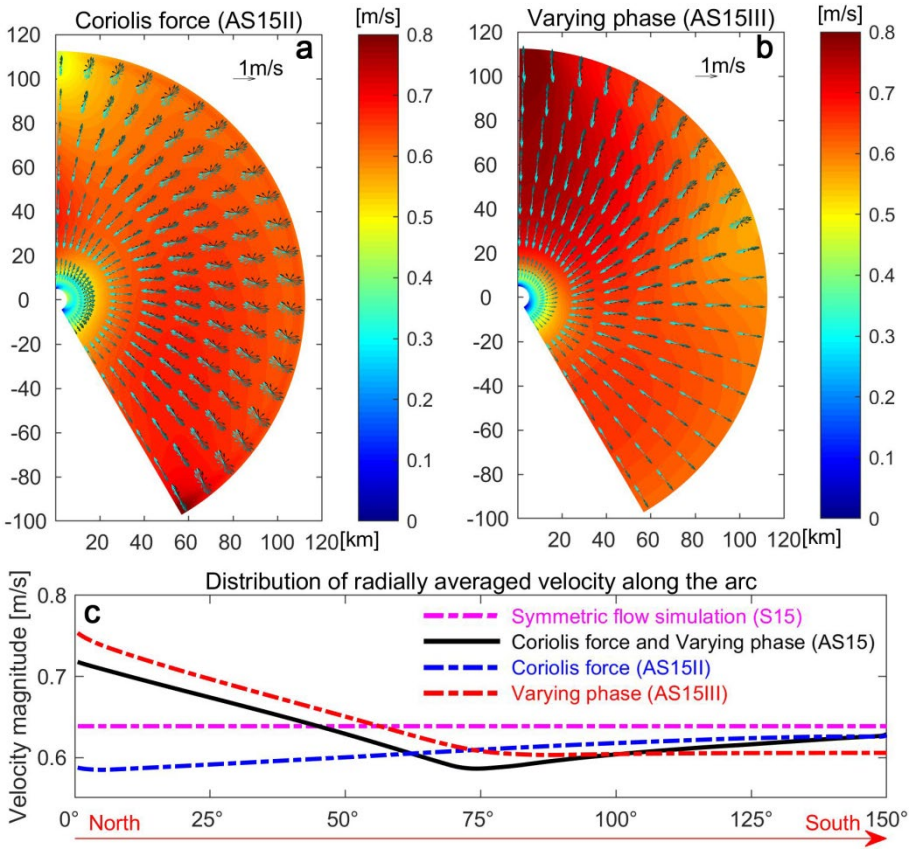

Figure 9. a) Peak velocity distribution in simulation AS15II. b) Peak velocity distribution in simulation AS15III. The tidal current vectors are displayed as arrows. c) Distribution of radially averaged velocity along the arc in simulation S15,AS15, AS15II and AS15III.

4.2 Idealized asymmetric flow simulations

In the previous section we determined that bottom slope controls the location of the maximum velocity band in a convergent coastline, with the maximum velocity band moving onshore when the bottom is tilted. The asymmetric hydrodynamic simulations (with Coriolis force and varying phase) show that the radial distribution of tidal prism is similar to that of the symmetric flow simulations, and also weakly dependent of bottom slope (Figure 5a). Thus, also in this case the bottom slope controls the location of maximum velocity as in the symmetric simulations (Figure 5b). The tangentially averaged peak velocity is maximum at the arc located 47 km from the apex for a bottom slope of 0.00015 (hereinafter referred to as arc47, see in Figure 8a). Tidal distortion increases from the northern part to the southern part in simulation AS15, characterized by an increase in M4/M2 ratio and an increasing sea-surface phase difference (2M2-M4) from 25° at the north end to 36° at the south end

along arc47.

The varying phase and Coriolis force give rise to an asymmetric flow pattern in the domain (Figure 8a). To study the asymmetric flow pattern between the northern and southern parts, we calculate the averaged peak velocity along each radius and then show the distribution of these averaged values along the arc direction (hereinafter referred to as "distribution of radially averaged velocity along the arc"). Similarly, we compute the water volume exchanged in a radial direction during both flood and ebb. During flood most of the water enters from the northern part while during ebb a fraction of the discharge is diverted to the southern part (Figure 8b). As a result, the distribution of radially averaged velocity along the arc is higher in the northern part. Even the peak velocity along arc47 is higher in the northern part near the west boundary, where we should therefore expect deep incision (Figure 8b).

To better understand what process is responsible for the increase in velocity in the northern part, we separately simulate the tidal flow subject to the Coriolis force (scenario AS15II) and varying phase (scenario AS15III). The Coriolis force deflects the tidal flow and leads to stronger flow in the southern area (Figure 9a). Compared to the symmetric simulation, the magnitude of radially averaged velocity consistently decreases in this scenario (Figure 9c). The varying phase along the northern half of the open boundary results in higher flow velocities in the north, especially near the west boundary where the tidal flood occurs earlier; a uniform flow field takes place in the southern part driven by the constant phase along the southern half of the open boundary (Figure 9b,9c). Therefore, the tidal flow asymmetry triggered by the varying phase dominates over the flow asymmetry caused by the Coriolis force (Figure 9c).

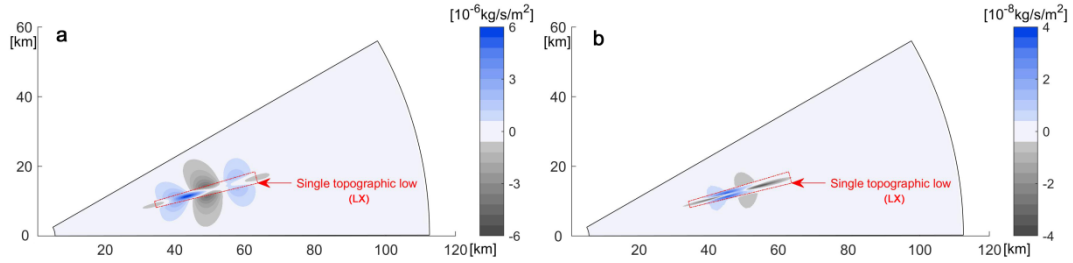

Figure 10. a) Difference in divergence of suspended load flux between scenario LX (single topographic low) and S15 (planar, sloping bottom). b) Difference in divergence of bed load flux between scenario LX (single topographic low) and S15 (planar, sloping bottom). Positive values mean increase in the divergence of sediment flux. We zoom in on the single topographic low and leave out the modeling domain with no difference in divergence.

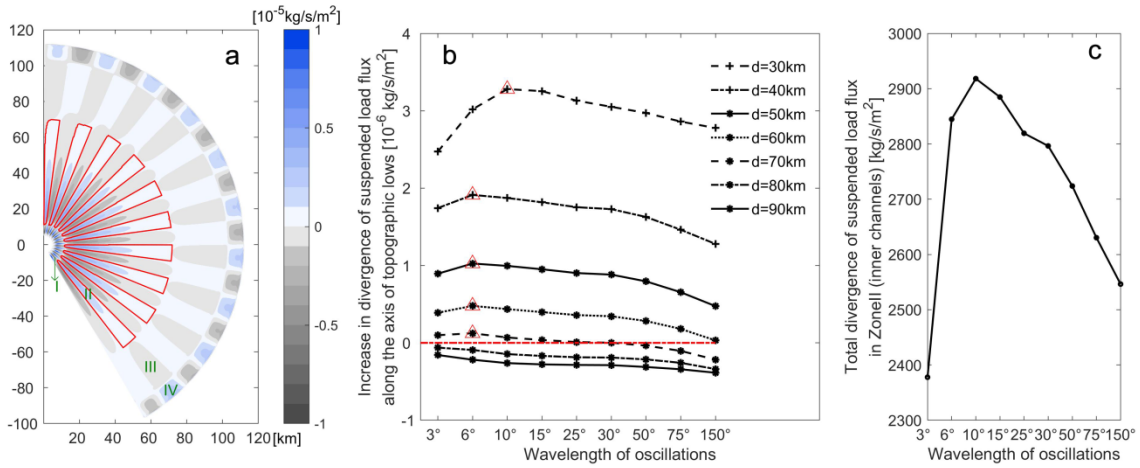

Figure 11. a) Difference in divergence of suspended load flux between scenario L4 (oscillating bottom) and S15 (planar, sloping bottom). Channels are classified in four different zones. Zone I and Zone III show potential convergence; Zone II and Zone IV show potential divergence. b) Increase in divergence of suspended load flux along the axis of radial small perturbations (topographic lows of scenarios L1-L9). Red triangles mark the largest divergence increase. c) Total divergence of suspended load flux in Zone II (inner channels).

4.3 Sediment transport in the idealized geometry

In the previous section we determined that there is a positive feedback between channel incision and flow redistribution. We then examine the sediment flux field around a single topographic low. The divergence of suspended sediment flux increases in a large part of the topographic low, suggesting sediment export and potential erosion. A decrease in flux divergence is present in nearby topographic highs. Only at the tips of the incision there is more convergence of sediment flux (Figure 10a). Bed load transport is both convergent and divergent in the topographic low (Figure 10b). Note that suspended sediment flux is two order of magnitude larger than bed load, and therefore dominant. Overall, flow concentration in the topographic low causes divergent fluxes that export sediments.

As an example of the impact of an oscillating seabed on sediment flux divergence, Figure 11a shows the change in the sediment flux divergence in scenario L4 (bottom oscillations with wavelength of 15°) versus the planar bed S15. Channels are divided in four different zones; the largest portion (Zone II) at an intermediate distance from the apex displays divergence. Convergence of sediment flux is only present in the Zone I near the apex and in the distal Zone III. In these areas the velocity is lower and sediment originating in Zone II is likely trapped (Figure 5c and Figure 6b). Note that in the RSRs the channels disappear near the apex (Zone I) and offshore (Zone III). Sediment flux divergence in Zone IV is caused by the open boundary conditions, since the mud concentration at the boundary was set to zero.

Figure 11b shows the increased divergence along the axis of channels as a function of oscillation frequency. Sediment divergence is maximum at a wavelength of 6-10 degrees at a distance of 30-70 km from the apex. We then quantify the sediment flushing capacity of channels by calculating the cumulative divergence in Zone II (inner channels). The total divergence peaks at a wavelength of 10° (Figure 11c). Therefore, incisions with a wavelength of 10° evacuate more sediment, possibly favoring erosion.

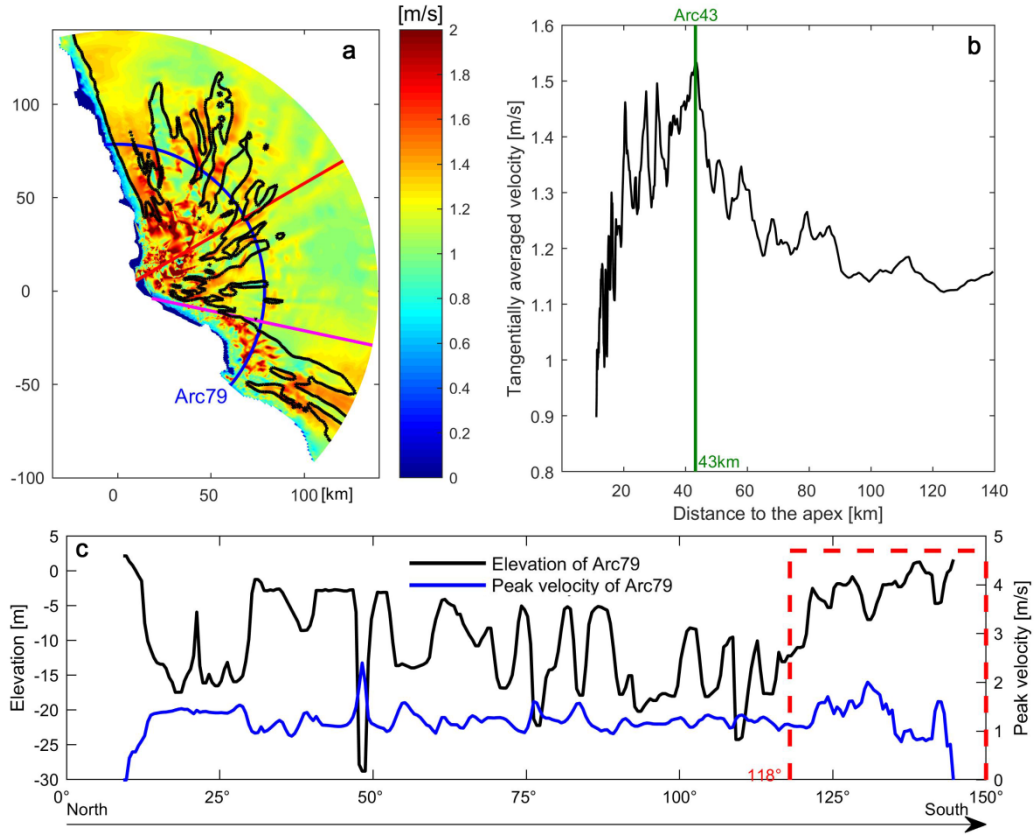

Figure 12. a) Peak velocity distribution resulting from high resolution simulations with the RSRs bathymetry. The black line indicates the 10m depth contour line. The position of arc79 (the arc located 79km away from the apex) is shown by the blue line. The red line shows the boundary between the northern and southern part. The magenta line indicates the 118° radius. b) Radial distribution of tangentially averaged velocity. c) Bed elevation and peak velocity along arc79.

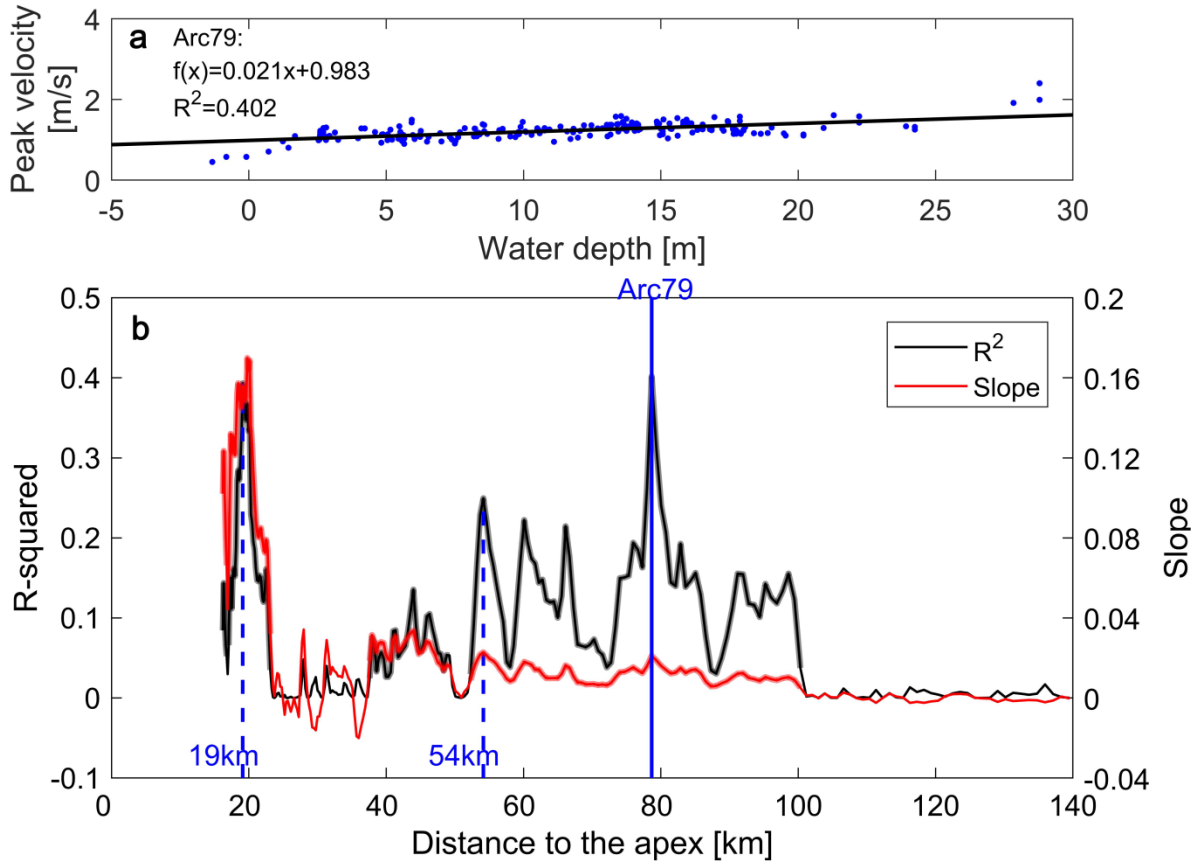

Figure 13. a) Relationship between peak velocity and water depth of arc79 (blue dots). The black line represents the linear regression line. The regression coefficients and the square of correlation coefficient (R^2) are shown in the upper left. b) Radial distribution of slope and R^2 of the linear regression line for each arc. The black line shows the R^2 distribution for each arc and the red line shows the regression slope for each arc. The regression coefficients significant with $p < 0.05$ are indicated by thicker lines.

4.4 Tidal hydrodynamics in the RSRs

Our idealized simulations suggest that the initiation of radial incisions is inherently linked to a positive feedback between depressions and flow redistribution. We then test whether a similar relationship between bathymetry and tidal flow is also present in the RSRs.

The 10m depth contour is closer to the coastline in the northern part of the RSRs. In this area the water becomes deeper offshore (Figure 1b). High velocity occurs near the northern coastline, which indicates concentration of tidal discharge (Figure 12a). Thus, the flow asymmetry detected by our idealized simulations is also confirmed when considering a simulation with real topography and 13 tidal constituents. The radial distribution of tangentially averaged velocity increases in the landward part of the RSRs, reaching a peak 43km away from the apex and then decreases seaward (Figure 12b). This peak in velocity is situated near the maximum velocity zone identified in the idealized simulations (Figure 5b).

Figure 12c shows the bed elevation along arc79 and the corresponding peak velocity during two spring tidal cycles. The velocities are higher in the channels than on the adjacent ridges, indicating

flow concentration. The flow velocity increases in the shallow area located between the radii 118° and 150° at the south end of arc79. Here, the shallow bathymetry of the shoals diverts the flow in the deeper parts, augmenting the velocity.

Flow concentration in the channels keeps them hydrodynamically active. To quantify what incisions are active in the system, we then measure the relationship between peak velocity and water depth of each arc as a function of distance to the apex. The shoals area between the radii 118° and 150° near the land boundary is excluded when we adopt linear regression between peak velocity and water depth, to avoid high velocities triggered by confined flow in the deeper parts. As an example, Figure 13a shows the scatter plot of arc79, as well as the linear regression line. The positive slope of the linear regression line of arc79 means that an increase in water depth generally leads to an increase of flow velocity. Figure 13b shows the regression slope and the R^2 coefficient for each arc. We test for the significance of the regression slopes different from zero. The regression coefficients which are significant with $p< 0.05$ are indicated by a thicker line in Figure 13b. The first peak in R^2 is reached 19km away from the apex, where the averaged water depth is 0.87m. Here flow is confined in the deeper parts in the shallow intertidal zone during flood and ebb, reaching high velocity (Fagherazzi and Mariotti, 2012). The next peaks of R^2 are reached between 54km to 79km away from the apex, corresponding to the position where velocity peaks in Figure 12b. Channels here are maintained flushed by flow concentration. No significant linear relationship between peak velocity and water depth is present in the distal part. This is because the redistribution of momentum from topographic highs to topographic lows is weak when the wavelength of bottom oscillations is too long (Figure 6b).

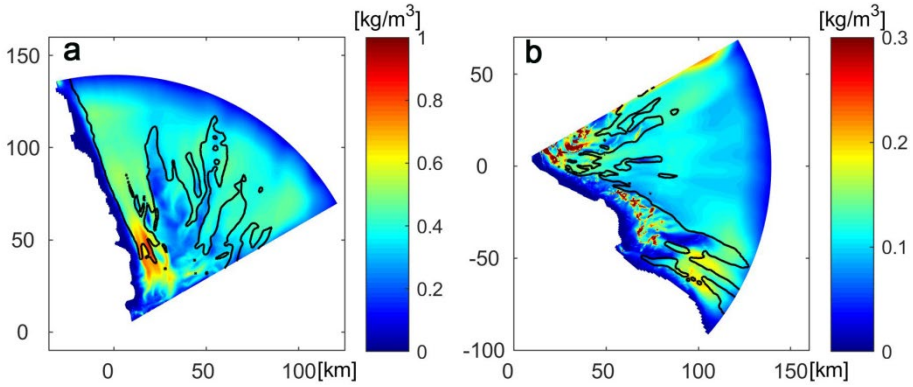

Figure 14. Distribution of mean suspended sediment concentration during two spring tidal cycles in the northern part (a) and southern part of RSRs (b). The black line indicates the 10m depth contour line.

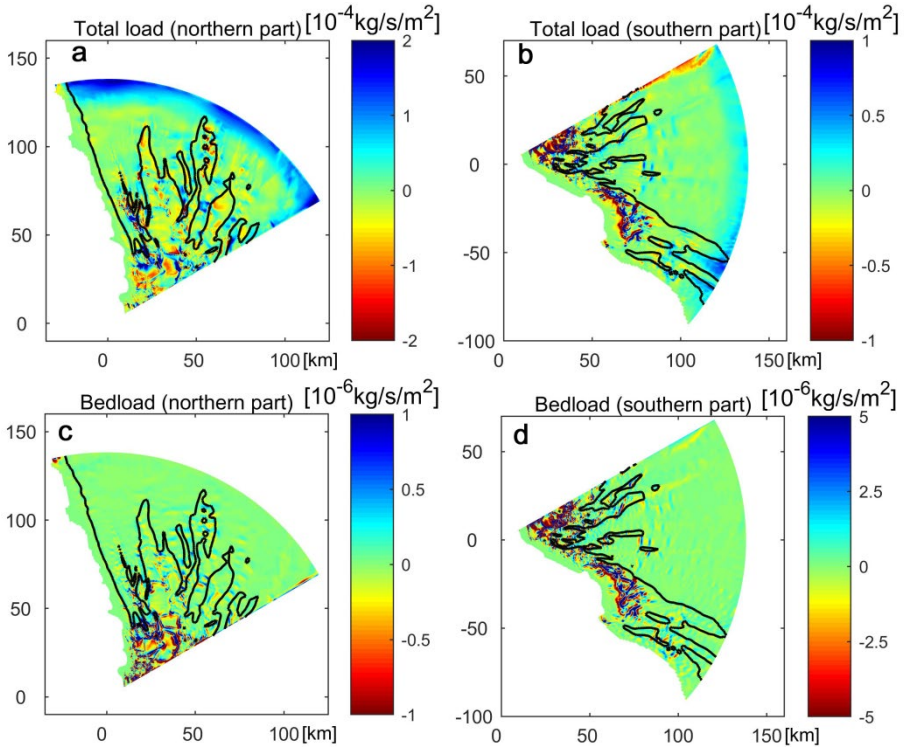

Figure 15. Sediment flux divergence for total load in the northern part (a) and southern part (b). Sediment flux divergence for bedload in the northern part (c) and southern part (d). Positive values mean divergence of sediment flux, and therefore erosion. The black line indicates the 10m depth contour line.

424

425

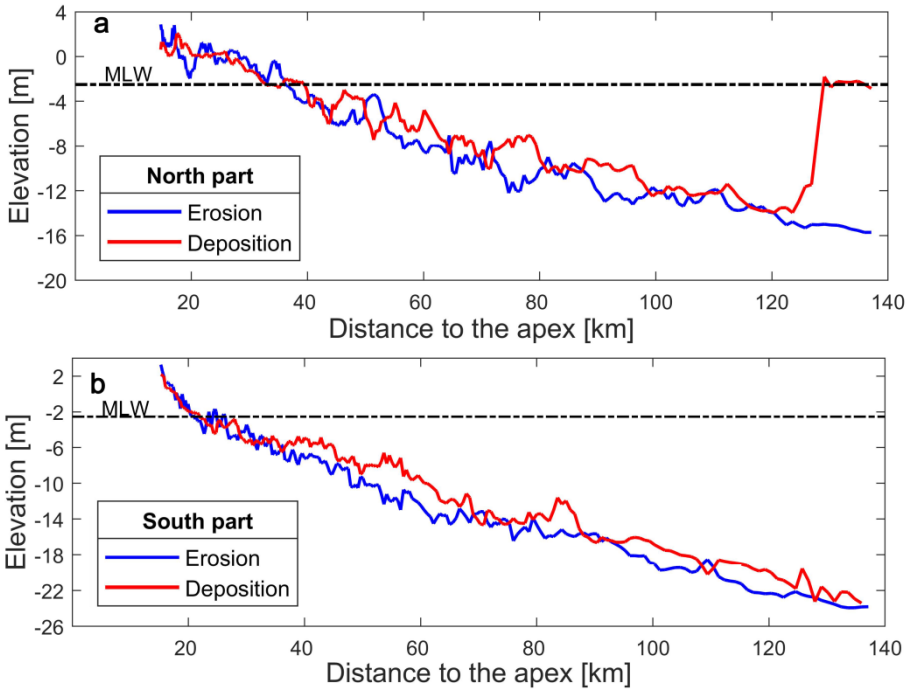

Figure 16. a) Radially distribution of the averaged bed elevation of locations under potential erosion (blue line) or deposition (red line) in the northern part (a) and southern part of RSRs (b). We report the mean low water level (MLW).

4.5 Sediment transport in the RSRs

Both suspended load and bed load fluxes are included when calculating the sediment flux divergence field in the RSRs. We define suspended load as the sum of both mud and sand suspended transport, while the bed load only consists of sand transport. Because of concentrated water flow, channels are characterized by a suspended sediment concentration higher than nearby ridges (Figure 14). Patterns of sediment flux divergence after two spring tides indicate elongated zones of sediment divergence (potential erosion) in the channels. Sediment fluxes converge on most ridges, likely triggering widespread deposition, while divergence occurs only in small-scale areas across the ridges (Figure 15a, 15b). Almost all areas in the distal part suffer potential erosion because the mud concentration at the open boundary was set to zero.

The pattern of sediment flux divergence for bed load presents both divergence and convergence in localized zones. Sediment flux divergence for total load is up to two order of magnitude than sediment flux divergence for bed load in the northern part, and one order of magnitude in the southern part (Figure 15). This means total load is significantly higher than bed load, with suspended load dominating sediment transport in the RSRs.

We report the averaged bed elevation of locations subject to sediment convergence (red line) or divergence (blue line) along each arc as a function of distance to the apex (Figure 16). we exclude the areas between the radii 118° and 150° when computing the averaged bed elevation of convergent and divergent fluxes in the southern part. The averaged bed elevation of areas under potential erosion is generally lower than those under deposition in both northern and southern parts, because most channels are active capturing momentum and discharge (Figure 13b). This can possibly lead to deeper incisions in the channels and accretion on the shoals.

Localized channel accretion and shoal erosion takes place within the first 40 km away from the apex. This area is characterized by overlapping zones of sediment divergence and convergence (Figure 15), and a small difference between the averaged bed elevation of erosion and deposition (Figure 16). These results indicate that the area is likely in dynamic equilibrium, with processes favoring incision balanced by processes that smooth the bathymetry. Numerical experiments with a single incision indicate that near the tip there is more convergence of sediment flux (Figure 10a) and low velocity (Figure 7a). The sediment flushed from the channels is therefore deposited near the apex, favoring the formation of shoals. Note that channels cannot extend near the apex because the tidal prism sharply decreases when the bottom elevation is above mean low tide. Wind waves, not considered herein, can also smooth the bathymetry favoring the formation of extensive shoals. All these processes can locally counteract channel formation, leading to a bathymetry in dynamic equilibrium in which incisions are suppressed.

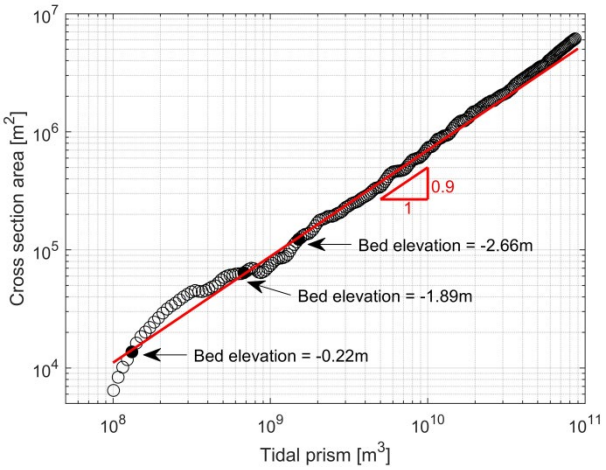

Figure 17. Tidal prism, P, versus cross section area, A, for arc sections with a distance from the apex larger than 20 km. The red line shows the power-law: $A = k\ P^{\partial}$, with $\partial = 0.9$ and k=0.0007. The average bed elevation of three arcs is also reported.

461
462

4.6 P-A relationship in the RSRs

463 464 465 466 467 468 469 470 471 472 473 474 475 476 477

The geomorphic law relating tidal prism, P, to channel cross section area, A, in the form of $A = k\ P^{\partial}$, is common in tidal landscapes (D'Alpaos et al., 2010; Friedrichs and Perry, 2001; Zhou et al., 2016). Mimicking this equation, here we analyze the relationship between the cross sectional area below mean sea level along each arc of the RSRs and the tidal prism flowing across it. The tidal prism is defined as the volume of water exchanged between mean high water and mean low water during a spring tide and it is expressed here as a function of distance from the apex. At intermediate locations, the total cross sectional area of each arc and the corresponding tidal prism satisfies a power-law with an exponent of 0.9 typical of tidal inlets (Figure 17).

The *P-A* relationship is not satisfied in the shallow intertidal zone near the apex, where the cross-sectional area is larger than expected. Wave-induced sediment resuspension occurs in shallow water (Fagherazzi et al., 2006), likely keeping the areas near the apex at lower elevation. Moving offshore the water depth generally increases while the incisions disappear. Eventually the bottom topography becomes unaffected by the tidal prism. This can be seen in Figure 17, where the cross sectional area along each arc grows more than the tidal prism in the distal part.

478

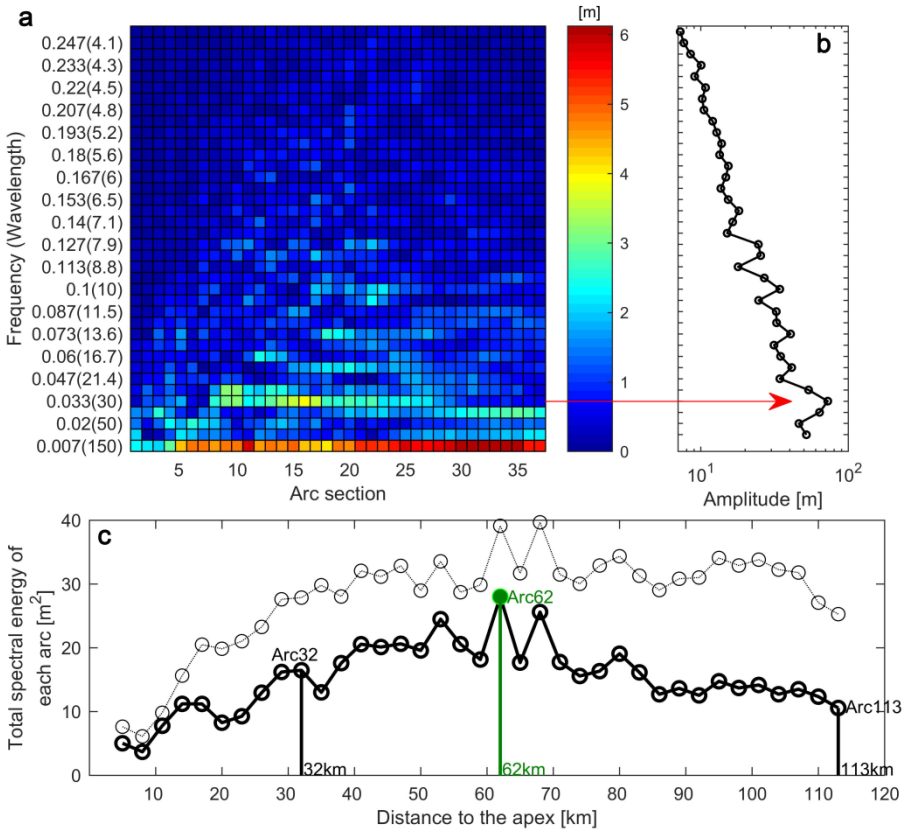

Figure 18. a) Single-sided amplitude spectrum of 37 arc transects resulted from the 1D fft. Y-axis is labeled both as frequency (1/degree) and corresponding wavelength in brackets (degrees). b) Total amplitude spectrum for each frequency. c) Radial distribution of total energy of each arc transect (dotted line), radial distribution of total energy excluding the wavelength of 150° (solid line).

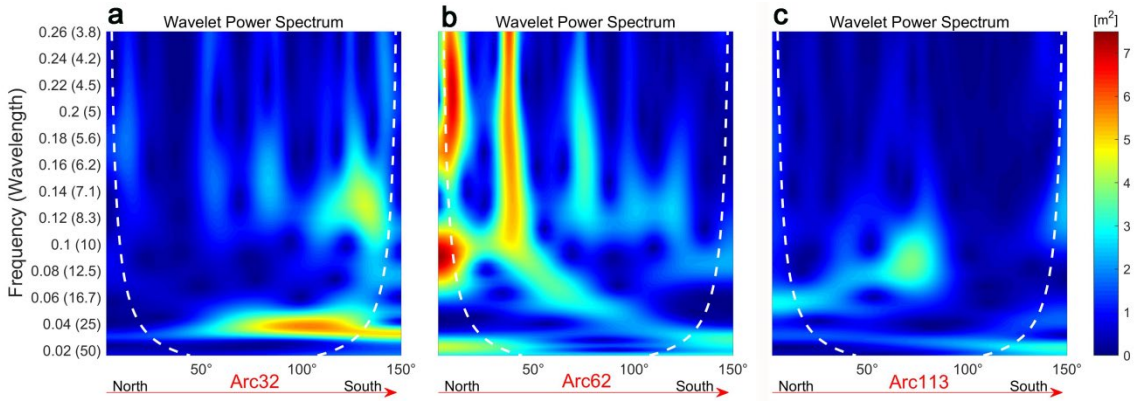

Figure 19. Wavelet power spectrum of arc32, arc62 and arc113 shown in Figure 18c. The white dash line indicates the edge effects occurring in the cone of influence.

4.7 Bathymetric analysis of the RSRs

We use Fourier analysis to study the bathymetry of the RSRs, which presents typical rhythmic bedforms in a fan-shaped basin. The seabed surface is not perfectly periodic, thus the spectral power

spreads over a range of wavelengths (Figure 18a). The lowest frequency, with wavelength 150 degrees, represents the large-scale shelf bathymetry, characterized by deep water in the central part and shallow water at the end-points of each arc transect. As a result, the power peaks at the wavelength 150 degrees, with increasing power values moving offshore. Apart from the lowest frequency (wavelength 150 degrees), there are some notable spectrum peaks at wavelength 25 to 37.5 degrees (Figure 18b). This indicates that on average the bottom is characterized by a quasiperiodic channels-ridges structure with characteristic wavelength ranging between 25 to 37.5 degrees. The characteristic range of wavelengths is comparable to the dominant wavelengths resulting from the numerical stability analysis (between 10 to 15 degrees in Figure 6b).

According to the discrete form of the Parseval's theorem, the total spectrum power in the frequency domain is equal to the variance of the signal in the space domain, if the signal has zero mean. Because we are interested in the variance of the seabed elevation sculpted by rhythmic channels, we exclude the wavelength 150 degrees, which is likely affected by the geological history of the inner shelf. The total energy of each arc transect first increases and then decreases moving offshore. This trend is accompanied by slight fluctuations, with the peak value taking place at 62km from the fan apex (Figure 18c). Therefore, along this arc section we encounter the largest variations in bathymetry and the deepest incisions. Note that this location is close to arc47 in the idealized asymmetric simulations, where maximum tangentially averaged velocity occurs (Figure 5b, 8a). High energy bottom oscillations mostly occur between 40km to 70km from the apex.

Wavelet analysis is further applied to arc32, arc62 and arc113 in order to identify spatial variations in the oscillations (Figure 19). Wavelengths between 25 to 37.5 degrees display a continuous high energy along these arcs and thus can be effectively measured by DFT. These wavelengths represent the large-scale oscillations of the bathymetry affecting the entire system (Figure 18). For the most energetic arc section, (arc62 62km from the fan apex), the largest nonstationary undulations are present for a wavelength between 4.5 to 11 degrees near the west boundary in the northern part. Here a deeply incised channel occurs, in correspondence to the location of maximum velocity shown in the asymmetric simulations (Figure 8a).

The low energy along the northern part of arc32 denotes large nearshore shoals, while deep channels-ridges oscillations with wavelength between 25 to 30 degrees are present in the southern part. A nonstationary peak in the middle part of arc113 is identified, which indicates a large scale bathymetric discontinuity, separating shallow water depths in the northern part from deep water depths in the southern part. These local topographic characteristics may be the result of differences in sediment supply and characteristics in the RSRs (Wang et al., 2012).

5. Discussion

In coastal tidal environments, tidal prism, its related peak velocity and shear stresses are crucial to sediment transport and hence morphodynamic evolution (Zhang et al., 2018; Donatelli et al., 2018). To explore the connections between tidal prism, peak velocity and the morphology of the RSRs in China we have carried out a morphometric analysis of the bathymetry, hydrodynamic and sediment transport simulations in an idealized fan-shaped basin, and high resolution simulations with the real bathymetry and tidal forcing. Some other studies have investigated the hydrodynamics, sediment transport and morphology in parts of the RSRs (Wang et al., 2019; Xing et al., 2012; Xu et al., 2016). However, this study is one of the few that focuses on the morphometric characteristics of the entire channels-ridges system and explores possible underlying controls of geomorphic processes.

The hydrodynamics and sediment transport of channel incisions are inherently linked to bottom bathymetry. Tidal channelization is triggered by flow concentration in incipient incisions (Fagherazzi and Furbish, 2001). Mariotti and Fagherazzi (2013) show that autogenic channelization occurs during tidal flats evolution, with a net export of sediment from the channels to the nearby tidal flat. Here we show that a similar mechanism is likely responsible for channel formation in a large and convergent tidal system. Our idealized simulations indicate that small perturbations of the initially unchannelized bottom surface cause higher velocities in the troughs, facilitating instability and leading to channel formation (Figure 6a). In a mature channel-ridge system, velocity concentration in the channels is still present, due to the redistribution of flow from the ridges to the channels (Figure 13). Because of higher velocity leading to scouring, tidal channels are characterized by a suspended sediment concentration higher than nearby ridges (Figure 14). As a result, the ridges-channels configuration can be maintained in time (Figure 15). A recent study based on both numerical simulations of sediment transport and observations in the RSRs indicates continuous sediment accretion on the major ridges and erosion in adjacent channels (Yao et al., 2018).

In a convergent coastal system having gentle sloping bottom, high velocities develop at an intermediate distance from the apex (Figure 5c). This is because the tidal prism is too small near the shore, reducing tidal discharges, while the water depth is too large offshore thus reducing tidal velocities. Eventually, the tidal velocity is so low in the distal part that the channels-ridges pattern disappears (Figure 1b, 18c).

By analyzing the bathymetry of the RSRs, we have shown that the deepest channel incisions are present along the arc located 62km from the apex (Figure 18c). Hydrodynamic simulations in an idealized basin with a bottom slope of 0.00015, similar to the averaged bottom slope of the RSRs, indicate that the most incised channels developed near the arc with the maximum value of tangentially averaged peak velocity. This arc is located at 47km from the apex (Figure 5b, 8a). We thus believe that the maximum velocity band has a strong control on the final morphological configuration because high flow velocities and bed shear stresses are decisive for the initiation and maintenance of channel incisions. More incised channels develop and can be kept flushed in the maximum velocity zone.

Our high resolution simulations with the real topography show that high velocities are present in the deep water bodies near the north coastline (Figure 12a). This flow concentration is mainly ascribed to the characteristics of the dominant semidiurnal tidal constituent M2 in the South Yellow Sea. The phase lag of the M2 harmonic facilitates more tidal flow exchange in the northern part compared to the southern one, likely leading to scour in the channels located to the north. The 10m depth contour line in the north is adjacent to the coastline and reflect the existence of wide channels, as well as the deepest channel incision in the offshore part (Figure 19b). These topographic features are inherently linked to the underling properties of the M2 tide.

Tidal asymmetry can affect sediment transport, hence the bottom slope of the basin (Aubrey and Speer, 1985). In a flood dominated system, ebb currents are incapable to flush out the incoming sediments, leading to a net import of material and widespread deposition at the basin head where flows are weak. Therefore, the modern bottom slope may be larger than the ancient one when the channels and ridges of the RSRs started forming. The band of maximum velocity might have moved inland, leaving behind highly incised channels (Figure 5b). In the long-term, the location of the deepest channels would adjust to the location of the maximum velocity band, because high velocities are needed to maintain the channels flushed of sediments.

Our numerical stability analysis also sheds light on the selective mechanism responsible for the

formation of radial tidal channels. The dominant perturbation wavelength (10°-15°) of bottom topography triggers the maximum increase in velocity in troughs and thus favors channel formation (Figure 6, Figure 11). Channels that develop too close to each other compete for tidal discharge, so that one is eventually abandoned. On the other hand, a very high perturbation wavelength of bottom topography does not lead to sufficient flow concentration. In this case the velocity decreases in the perturbation troughs because of the higher water depths. This negative feedback prevents the development of bottom perturbations and suppresses the channelization process in the distal part of a large and convergent tidal system.

In the developing phase, nearby incisions compete for the total amount of discharge so that few become large enough to convoy most of the flow whereas the remaining are abandoned. This initial number of incisions could decrease in time if the system is perturbed. The RSRs is a dominated by tide, but it is also subject to wind waves (Zhang et al., 2017). Wind waves can redistribute sediments, eroding ridges and silting nearby channels. Waves can therefore suppress incisions, reducing the number of channels. Because of disturbances not accounted in our framework, the wavelength of bottom oscillations tends to be higher than 10-15 degrees. More research is clearly needed to determine the effect of wind waves on this system.

Spatial variability of substrate characteristics is common in the RSRs because of different sediment sources contributing to the system in different historical periods (Rao et al., 2015; Wang et al., 2012). The northern part of the RSRs received abundant suspended sediments from the Old Yellow River Mouth (Zhou et al., 2014a). The deposition of these sediments formed wide shoals likely burying small tidal channels. This deposition enhanced the concentration of momentum in the surviving channels, increasing their incision. Regional variations in sediment availability can also promote the asymmetric layout of the modern channels and ridges (Xu et al., 2016). As a large-scale tidal channels system, the RSRs have evolved for several thousands of years to develop incisions, with the cross-section of each incision adjusting to tidal flow (Lu, 2002). This observation is corroborated by our results, indicating that tidal prism and incisions are strongly linked (Figure 17).

Large-scale periodic oscillations are common components of the shelf landscape, such as linear sand banks observed in the southern North Sea, the East China Sea and in the Thames Estuary, UK (Dyer and Huntley, 1999). Huthnance (1982a, b) first explained the processes controlling the convergence of sediment flux on sand ridges and the formation of periodic linear sand banks, based on simplified two-dimensional shallow water equations and a power-law sediment transport formula. The net upslope sediment flux is a result of the local current asymmetry generated by the bed slope, and the competition between upslope and downslope sediment transport selects the particular wavelength with the maximum growth rate. This might be true in coarse-grained environments where bed load dominates, while if suspended load of fine particles is crucial such as in the RSRs, the exchange of sediment between channels and ridges can be independent of bottom slope. Tidal advection in conjunction with spatial variations in SSC lead to a net flux of sediments from areas of high tidal energy toward areas of low tidal energy. In the RSRs sediment flux divergence and convergence is mainly controlled by the suspended sediment load, which is two orders of magnitude higher than bed load in the northern part and one order of magnitude higher in the southern part (Figure 15). The spatial distribution of sediment flux divergence indicates that sediment exchange takes place between channels and ridges, leading to erosion in most channels and accretion in nearby ridges.

Physical agents that acted during the post-glacial sea level rising may be essential for the formation of sand banks located in the inner- and mid-shelf (Dyer and Huntley, 1999). Whereas in

coastal regions, where tides and waves are most effective in reworking sediments, bottom topography can adapt to physical processes at the decadal timescale (Zhang et al., 2018). The feedback between channel incisions and flow redistribution in the RSRs is an example of how tidal hydrodynamics redistribute the sediment and thus sculpt coastal landscapes. We believe that the identification and quantification of feedbacks between hydrodynamics and sediment transport is crucial in order to understand rhythmic patterns present in coastal landscapes.

6. Conclusions

In this research we reduced the morphology of radial tidal channels down to their simplest representation to detect the chief driving processes. A positive morphological feedback between channel incision and flow redistribution is responsible for the formation of the channels-ridges pattern in the RSRs, similar to other tidal incisions. A selection mechanism of bottom oscillations occurs, which favors a dominant wavelength leading to maximum flow concentration. Furthermore, high resolution simulations with the RSRs bathymetry demonstrates how a positive feedback between channel incisions and flow redistribution is present in the real system.

The following results were derived from our morphometric analysis of the RSRs:

(1) The *P-A* relationship, relating tidal prism and cross sectional area of the channels, holds, similarly to tidal inlets and intertidal channels.

(2) In an idealized, convergent basin the tidal prism increases moving offshore together with water depth. As a result, the tangentially average tidal velocity peaks at an intermediate location (at 47km for a bottom slope of 0.00015). The location with maximum velocity is close to the location of maximum incision in the RSRs (62 km from the apex).

(3) Tidal flow asymmetry caused by the offshore tidal phase lag leads to stronger tidal flows in the northern part of the basin. This is likely responsible for the asymmetric pattern of channels, with the deepest incisions located near the northern coastline.

(4) A perturbation analysis carried out in a planar, convergent basin indicates that periodic bottom oscillations with an angular frequency between 10° to 15° produce maximum flow concentration in troughs. This frequency is comparable to the frequencies with highest spectral energy in the RSR bathymetry (between 25 to 37.5 degrees).

We therefore conclude that the RSRs display morphometric characteristics similar to other tidal incisions, as tidal inlets and intertidal channels. The tidal prism and its variability in space play therefore a strong control on the morphology of radial sand ridges.

Acknowledgments

This research was supported by the National Natural Science Foundation of China (No.51979096), the National Science & Technology Pillar Program of China (No. 2012BAB03B01), and the China Scholarship Council (No. 201706710103). S.F. was partly funded by the U.S. National Science Foundation award 1832221 (VCR LTER) and 1637630 (PIE LTER). We would also thank the Editor Stuart Lane, the Associate Editor, John Shaw and three anonymous reviewers for their constructive comments.

Data Availability Statement

Research data are not shared.

References

Allen, J.I., Somerfield, P.J., Gilbert, F.J. (2007). Quantifying uncertainty in high-resolution coupled hydrodynamic-ecosystem models. Journal of Marine Systems, 64(1-4), 3-14.

Aubrey, D.G., Speer, P.E. (1985). A study of non-linear tidal propagation in shallow inlet/estuarine systems Part I: Observations. Estuarine, Coastal and Shelf Science, 21(2), 185-205.

Blondeaux, P., Seminara, G. (1985). A unified bar-bend theory of river meanders. Journal of Fluid Mechanics, 112(157), 449-470.

Cazenave, P.W., Dix, J.K., Lambkin, D.O., Mcneill, L.C. (2013). A method for semi-automated objective quantification of linear bedforms from multi-scale digital elevation models. Earth Surface Processes and Landforms, 38(3), 221–236.

D'Alpaos, A., Lanzoni, S., Marani, M., Fagherazzi, S., Rinaldo, A. (2005). Tidal network ontogeny: Channel initiation and early development. Journal of Geophysical Research, 110, F02001.

D'Alpaos, A., Lanzoni, S., Marani, M., Rinaldo, A. (2010). On the tidal prism - channel area relations. Journal of Geophysical Research, 115, F01003.

De Swart, H.E., Zimmerman, J.T.F. (2009). Morphodynamics of tidal inlet systems. Annual Review of Fluid Mechanics, 41, 203-229.

Donatelli, C., Ganju, N. K., Zhang, X., Fagherazzi, S., Leonardi, N. (2018). Salt marsh loss affects tides and the sediment budget in shallow bays. Journal of Geophysical Research: Earth Surface, 123, 2647-2662.

Dyer, K. R., Huntley, D. A. (1999). The origin, classification and modelling of sand banks and ridges. Continental Shelf Research, 19, 1285-1330.

Egbert, G.D., Bennett, A.F., Foreman, M.G. (1994). TOPEX/POSEIDON tides estimated using a global inverse model. Journal of Geophysical Research: Oceans, 99(C12), 24821–24852.

Egbert, G.D., Erofeeva, S.Y. (2002). Efficient inverse modeling of barotropic ocean tides. Journal of Atmospheric and Oceanic Technology, 19(2), 183-204.

Fagherazzi, S. (2008). Self-organization of tidal deltas. Proceedings of the National Academy of Sciences, 105, 18692-18695.

Fagherazzi, S., Bortoluzzi, A., Dietrich, W.E., Adami, A., Lanzoni, S., Marani, M., Rinaldo, A. (1999). Tidal networks: 1. Automatic network extraction and preliminary scaling features from digital terrain maps. Water Resources Research, 35(12), 3891-3904.

Fagherazzi, S., Carniello, L., D'Alpaos, L., Defina, A. (2006). Critical bifurcation of shallow microtidal landforms in tidal flats and salt marshes. Proceedings of the National Academy of Sciences, 103, 8337-8341.

Fagherazzi, S., Furbish, D.J. (2001). On the shape and widening of salt marsh creeks. Journal of Geophysical Research, 106(C1), 991-1003.

Fagherazzi, S., Hannion, M., D'Odorico, P. (2008). Geomorphic structure of tidal hydrodynamics in salt marsh creeks. Water Resources Research, 44, W02419.

Fagherazzi, S., Mariotti, G. (2012). Mudflat runnels: Evidence and importance of very shallow flows in intertidal morphodynamics. Geophysical Research Letters, 39, 14402.

Fagherazzi, S., Sun, T. (2004). A stochastic model for the formation of channel networks in tidal marshes. Geophysical Research Letters, 31, L21503.

Fagherazzi, S., Wiberg, P.L., Howard, A.D. (2003). Tidal flow field in a small basin. Journal of Geophysical Research, 108(C3), 3071.

Friedrich, C. T., Aubrey, D. G. (1988). Non-linear tidal distortion in shallow well-mixed estuaries: A synthesis. Estuarine, Coastal and Shelf Science, 27, 521-545.

706 Friedrichs, C.T., Perry, J.E. (2001). Tidal salt marsh morphodynamics: A synthesis. Journal of Coastal Research,(27), 7-37.
707 Guo, L. (2014), Modeling estuaine morphodynamics under combined river and tidal forcing. Delft, Delft Univerisity of
708 Technololgy.
709 Hibma, A., De Vriend, H.J., Stive, M. (2003). Numerical modelling of shoal pattern formation in well-mixed elongated
710 estuaries. Estuarine, Coastal and Shelf Science, 57(5-6), 981–991.
711 Huthnance, J.M. (1982a). On one mechanism forming linear sand banks. Estuarine, Coastal and Shelf Science, 14(1), 79-
712 99.
713 Huthnance, J.M. (1982b). On the formation of sand banks of finite extent. Estuarine, Coastal and Shelf Science, 15(13),
714 277-299.
715 Lu, P. (2002), The system of tidal inlet and the response to environment. Nanjing, Nanjing Normal University. (In Chinese)
716 Luan, H.L., Ding, P.X., Wang, Z.B., Ge, J.Z. (2017). Process-based morphodynamic modeling of the Yangtze Estuary at a
717 decadal timescale: Controls on estuarine evolution and future trends. Geomorphology, 290, 347-364.
718 Marciano, R., Wang, Z.B., Hibma, A., De Vriend, H.J. (2005). Modeling of channel patterns in short tidal basins. Journal
719 of Geophysical Research, 110, F01001.
720 Mariotti, G., Fagherazzi, S. (2013). A two-point dynamic model for the coupled evolution of channels and tidal flats.
721 Journal of Geophysical Research: Earth Surface, 118(3), 1387-1399.
722 Murray, A.B. (2007). Reducing model complexity for explanation and prediction. Geomorphology, 90, 178-191.
723 Myrick, R.M., Leopold, L.B. (1963). Hydraulic geometry of a small tidal estuary U.S. Geological Survey Professional
724 Paper, 422B, 12-18.
725 Parker, G. (1976). On the cause and characteristic scales of meandering and braiding in rivers. Journal of Fluid Mechanics,
726 76(3), 457-480.
727 Partheniades, E. (1965). Erosion and deposition of cohesive soils. Journal of the Hydraulics Division, 91(1), 105-139.
728 Perron, J.T., Kirchner, J.W., Dietrich, W.E. (2009). Spectral signatures of characteristic spatial scales and nonfractal
729 structure in landscapes. Journal of Geophysical Research, 113, F04003.
730 Qian, X., Chen, Y., Zhang, C., Pan, Y., Himangshu, D. (2015). Radial tidal current field in a semi-enclosed rectangular
731 basin: Formation and evolution. Chinese Journal of Oceanology and Limnology, 33(4), 1085-1099.
732 Rao, W., Mao, C., Wang, Y., Su, J., Balsam, W., Ji, J. (2015). Geochemical constraints on the provenance of surface
733 sediments of radial sand ridges off the Jiangsu coastal zone, East China. Marine Geology, 359, 35-49.
734 Schramkowski, G.P., Schuttelaars, H.M., De Swart, H.E. (2002). The effect of geometry and bottom friction on local bed
735 forms in a tidal embayment. Continental Shelf Research, 22, 1821-1833.
736 Schuttelaars, H.M., De Swart, H.E. (1999). Initial formation of channels and shoals in a short tidal embayment. Journal of
737 Fluid Mechanics, 386, 15-42.
738 Seminara, G. (1998). Stability and morphodynamics. Meccanica, 33, 59-99.
739 Seminara, G. (2009). Fluvial sedimentary patterns. Annual Review of Fluid Mechanics, 42, 43-66.
740 Stelling, G. (1983), On the construction of computational methods for shallow water flow problems. Delft, Delft University
741 of Technology.
742 Su, M., Yao, P., Wang, Z., Zhang, C., Stive, M.J.F. (2015). Tidal wave propagation in the Yellow Sea. Coastal Engineering
743 Journal, 57(3), 1550008.
744 Su, M., Yao, P., Wang, Z., Zhang, C., Stive, M.J.F. (2017). Exploratory morphodynamic hindcast of the evolution of the
745 abandoned Yellow River delta, 1578–1855 CE. Marine Geology, 383, 99-119.
746 Tao, J., Wang, Z.B., Zhou, Z., Xu, F., Zhang, C., Stive, M.J.F. (2019). A morphodynamic modeling study on the formation
747 of the large-scale radial sand ridges in the Southern Yellow Sea. Journal of Geophysical Research: Earth Surface, 124,
748 1742-1761.
749 Taylor, G.I. (1922). Tidal oscillations in gulfs and rectangular basins. Proceedings of the London Mathematical Society,

s2-20(1), 148-181.
Temmerman, S., Bouma, T.J., Van de Koppel, J., Van der Wal, D., De Vries, M.B., Herman, P.M.J. (2007). Vegetation causes channel erosion in a tidal landscape. Geology, 35(7), 631-634.
Torrence, C., Compo, G.P. (1998). A practical guide to wavelet analysis. Bulletin of the American Meteorological Society, 79(1), 61-78.
Van der Wegen, M., Roelvink, J.A. (2008). Long-term morphodynamic evolution of a tidal embayment using a two-dimensional, process-based model. Journal of Geophysical Research, 113, C03016.
Van Dijk, T.A.G.P., Lindenbergh, R.C., Egberts, P.J.P. (2008). Separating bathymetric data representing multiscale rhythmic bed forms: A geostatistical and spectral method compared. Journal of Geophysical Research, 113, F04017.
Van Rijn, L.C., 1993. Principles of sediment transport in rivers, estuaries and coastal seas (vol. 1006). Amsterdam, Aqua Publications,
Wang, Y., Wang, Y., Yu, Q., Du, Z., Wang, Z.B., Gao, S. (2019). Sand-mud tidal flat morphodynamics influenced by alongshore tidal currents. Journal of Geophysical Research: Oceans, 124, 3818-3836.
Wang, Y., Zhang, W., Huang, H., Chen, C. (2015). Review of studies on sources and transport of sediment in the Radial Sand Ridges. Advances in Science and Technology of Water Resources, 35(5), 59-67. (In Chinese)
Wang, Y., Zhang, Y., Zou, X., Zhu, D., Piper, D. (2012). The sand ridge field of the South Yellow Sea: Origin by river–sea interaction. Marine Geology, 291-294, 132-146.
Winterwerp, J.C., Maa, J., Stanford, L., Schoellhamer, D., 2007. On the sedimentation rate of cohesive sediment. In: Estuarine and Coastal Fine Sediments Dynamics INTERCOH 2003. Elsevier, pp. 209-226.
Xing, F., Wang, Y.P., Wang, H.V. (2012). Tidal hydrodynamics and fine-grained sediment transport on the radial sand ridge system in the southern Yellow Sea. Marine Geology, 291-294, 192-210.
Xu, F., Coco, G., Zhou, Z., Tao, J., Zhang, C. (2017). A numerical study of equilibrium states in tidal network morphodynamics. Ocean Dynamics, 67(12), 1593-1607.
Xu, F., Tao, J., Zhou, Z., Coco, G., Zhang, C. (2016). Mechanisms underlying the regional morphological differences between the northern and southern radial sand ridges along the Jiangsu Coast, China. Marine Geology, 371, 1-17.
Yang, S., Li, C., Jung, H.S., Lee, H.J. (2002). Discrimination of geochemical compositions between the Changjiang and the Huanghe sediments and its application for the identification of sediment source in the Jiangsu coastal plain, China. Marine Geology, 186, 229-241.
Yao, P., Su, M., Wang, Z.B., van Rijn, L.C., Zhang, C., Stive, M.J.F. (2018). Modelling tidal-induced sediment transport in a sand-silt mixed environment from days to years: Application to the Jiangsu coastal water, China. Coastal Engineering, 141, 86-106.
Yao, P., Wang, Z., Zhang, C., Su, M., Chen, Y., Stive, M.J.F., 2013. The genesis of the radial tidal current off the central Jiangsu Coast. In: Coastal Dynamics 2013. Bordeaux University, Arcachon, France, pp. 1947-1958.
Zhang, C., Zhang, D., Zhang, J., Wang, Z. (1999). Tidal current-induced formation—storm-induced change—tidal current-induced recovery. Science in China (Series D), 42(1), 1-12.
Zhang, W., huang, H., Wang, Y., Chen, D., Zhang, L. (2017). Mechanistic drifting forecast model for a small semi-submersible drifter under tide-wind-wave coupled conditions. China Ocean Engineering, 32(1), 99-109.
Zhang, X., Fagherazzi, S., Leonardi, N., Li, J. (2018). A positive feedback between sediment deposition and tidal prism may affect the morphodynamic evolution of tidal deltas. Journal of Geophysical Research: Earth Surface, 123, 2767-2783.
Zhou, L., Liu, J., Saito, Y., Zhang, Z., Chu, H., Hu, G. (2014a). Coastal erosion as a major sediment supplier to continental shelves: Example from the abandoned Old Huanghe (Yellow River) delta. Continental Shelf Research, 82, 43-59.
Zhou, Z., Coco, G., Townend, I., Olabarrieta, M., Wegen, M.v.d., Gong, Z., D'Alpaos, A., Gao, S., Jaffe, B.E., Gelfenbaum, G. (2016). Is "Morphodynamic Equilibrium" an oxymoron?. Earth-Science Reviews, 165, 257-267.
Zhou, Z., Olabarrieta, M., Stefanon, L., D'Alpaos, A., Carniello, L., Coco, G. (2014b). A comparative study of physical

and numerical modeling of tidal network ontogeny. Journal of Geophysical Research: Earth Surface, 119, 892-912.
Zhu, Y., Chang, R. (2001). On the relationships between the radial tidal current field and the radial sand ridges in the southern Yellow Sea: A numerical simulation. Geo-Marine Letters, 21(2), 59-65.